AIAA JOURNAL
Vol. 41, No. 12, December 2003

# Flow Visualization of Numerically Simulated Blast Waves Discharging from Open-Ended Duct

S. M. Liang* and H. Chen†
*National Cheng-Kung University, Tainan 701, Taiwan, Republic of China*

**In this study a high-resolution Euler solver is used to investigate the flowfields of different-intensity planar blast waves discharging from an open-ended duct. Acoustic waves and a vortex pair generated by blast/vortex interactions near the 90-deg sharp corner of the duct at different blast Mach numbers are studied in detail by using computational shadowgraghs, computational schlieren pictures, and computational interferograms. It is found that the schlieren technique provides a better method for the study of acoustic waves than the other two techniques. The number of sounds generated by blast/vortex interaction as well as its nature is dependent on the strength of the blast wave. Moreover, the mechanism of vorticity generation induced by blast-wave diffraction is explored. It is found that the compressibility term, the vorticity scaled down by the fluid dilatation, is more dominant than the baroclinic term in the vorticity transport equation during the second shock/vortex interaction. The compressibility term is mainly contributed by the rollup of the slipstream, but not by the fluid dilatation. The induced vortex pair caused by blast-wave diffraction rotates cyclically after the second shock/vortex interaction. The circulation (or strength) of the two vortices increases to a maximum value when the second shock begins to interact with the major vortex, and it decreases to a constant value when the second shock has moved far downstream.**

## I. Introduction

ENVIRONMENT protection issues have become important in recent years. Particularly, noise emitted from automobiles is a serious problem. Noise emitted from an internal combustion engine and an exhaust system can be classified as three types: turbulence noise, shell noise, and radiated noise. Turbulence noise results from turbulent mixing at the exhaust outlet. Shell noise results from wall vibration caused by the shock waves traveling through the exhaust system. These shock waves, along with acoustic waves emitted from the open end of the exhaust system, radiate noise and generate a complicated flow structure. In the past most papers related to radiated noise have focused on studies of shock/vortex interaction, one of the major sources of noise and closely related to some aerodynamic problems. However, pressure discontinuities in practical exhaust systems are better described as blast rather than shock waves. Because expansion waves follow the shock front of a blast wave, the flow phenomenon induced by blast/vortex interaction is more complicated than that induced by shock/vortex interaction. Thus, understanding the basic flow structure created by a planar blast wave discharging from an open-ended duct is a necessary step in the study of the more complex practical three-dimensional problem.

Typically, a blast wave caused by the rapid release of energy in gas consists of the primary shock front $S_1$, expansion wave, and second shock $S_2$, as shown in Fig. 1. Behind the primary shock front, flow properties such as pressure and density decrease rapidly because of the expansion waves. The process of planar blast wave discharging from an open-ended duct can be divided into two parts: first, the primary shock $S_1$ passes the corner and induces a vortex, and second, the second shock $S_2$ passes the corner and interacts with the induced vortex.

Hillier[1] numerically studied shock-wave diffraction at a 90-deg edge by solving the Euler equations. His computations were performed on a sufficiently refined mesh to ensure a good resolution of flow features that included the primary diffracting shock wave, the second shock wave, and a pair of vortex shocks. The numerical result of the Mach number of the calculated diffracted shock near wall, slipstream angle, second shock velocity, contact surface velocity, and vortex core velocity agreed well with experimental results. Yang et al.[2] analytically and computationally investigated the vortical flow induced by the interaction of a planar shock wave with a light-gas jet. They pointed out that the vorticity generated is mainly caused by the baroclinc effect of the misalignment of the pressure and density gradients.

Yates[3] described a method to construct equivalent interferograms, schlieren images, and shadowgraphs based on computed two and three-dimensional flowfields for ideal and real gases. The constructed images were compared with experimental images for several types of flow, including a ramp, a blunt body, a nozzle, and a reacting flow. All of the constructed images could be used for validation of computational fluid dynamics codes. Both schlieren images and shadowgraphs were helpful for flow visualization and to locate flow structure. Particularly, the interferograms provided quantitative flowfield information, including the density variation in a flowfield.

Yu and Grönig[4] developed a method for decreasing the attenuation of a shock wave emerging from an open-ended shock tube exit into a large free space with different exit geometries. This method might be used to improve the shock-wave technique for cleaning deposits on the surfaces in industrial equipments. Their experiment was carried out in a cylindrical open-ended shock tube with Mach number 3.5 and the initial pressure of 90 bar in the driver tube. The tube-exit geometry has three types: a plain tube exit, a tube exit with a ring shape, and a coaxial tube exit. An upwind, finite volume scheme based on Godunov's method as well as an adaptive unstructured triangular-mesh refining/coarsening algorithm was adopted to study the flow structure. Their numerical results agreed remarkably with the experimental data. It was found that the coaxial tube exit produced the strongest disturbances behind the diffracting shock wave, resulting in a stronger acoustic noise.

Inoue and Hattori[5] studied the detailed flowfields produced by the interactions between a single vortex or a pair of vortices and a shock wave by using the Navier–Stokes equations. They explored the basic nature of the sound pressure field for the case of a single vortex and then a pair of vortices. In their study the effect of the Reynolds number seemed insignificant. Kim and Setoguchi[6] performed an

---

Received 19 August 2002; revision received 14 April 2003; accepted for publication 8 August 2003.

*Professor, Institute of Aeronautics and Astronautics. Associate Fellow AIAA.

†Graduate Student, Institute of Aeronautics and Astronautics.

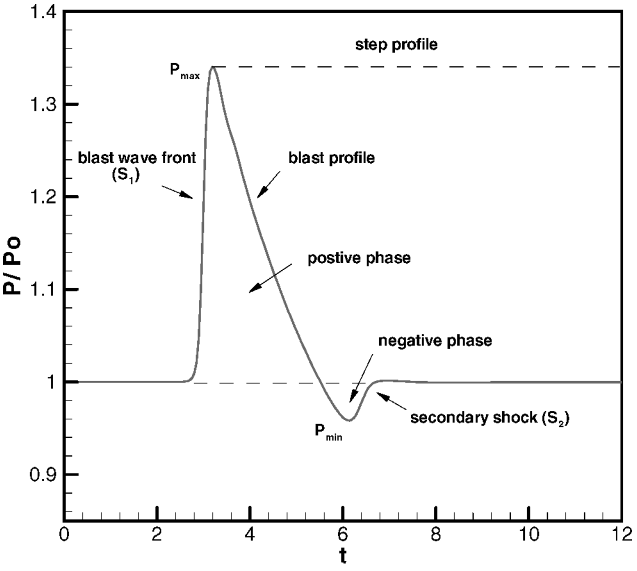

**Fig. 1 Typical blast-wave pressure profile.**

experiment using an open-ended shock tube with shock Mach number of 1.02–1.45 in order to characterize the impulse wave caused by a weak shock discharged from an open-ended duct with a baffle plate at downstream. They applied a total-variation-diminishing scheme in a conservative form to solve the Euler equations for the unsteady, axisymmetric flowfield. Their result showed that the baffle plate could affect the strength of the impulse wave when its diameter is less than three times the duct diameter. It was also found that for prediction of the impulse wave an aeroacoustical theory should be used only at a distance larger than four times the duct diameter.

Jiang and Takayama[7] demonstrated the effectiveness and reliability of a method proposed for validation of numerical solutions of complex flowfields including two-dimensional, axisymmetric, and three-dimensional flows. Images of these flowfields were constructed from numerical solutions based on the principle of experimental flow visualization and compared with experimental interferograms. In particular, an efficient algorithm for three-dimensional density integration to create image that can be directly compared with experimental interferograms was proposed. The computational interferograms showed good agreement with experimental results through examining characteristic flow structures as well as comparing density differences.

Szumowski et al.[8] experimentally and theoretically studied a starting jet-wall interaction problem. The jet issuing from a shock tube was visualized by means of a schlieren system. The flow Mach number ranged from 0.65 to 1.14. It was found that the shock wave, after reflection at the wall, generated a toroidal sound wave caused by its interaction with a ring vortex. Their theoretical approach was based on the Euler equations by which they satisfactorily predicted the main flow characteristics. Abate and Shyy[9] reviewed experimental and numerical results to highlight the flow phenomena and the main physics associated with confined shocks undergoing a sudden expansion. The subjects they addressed include the time-accurate shock and vortex locations, flow structure, wall-shock Mach number, and effect of viscous dissipation on planar shock-front expansions for two- and three-dimensional sudden-expansion problems. Both numerical and experimental studies confirmed that the induced vortex in an axisymmetric case was convected farther downstream than that in the corresponding two-dimensional case. Their study indicated that the production of vorticity is closely related to the baroclinic torque in the vorticity transport equation. But they did not describe its detailed mechanism. A vortex was generated as the fluid exited at the sudden expansion, and vorticity generation was not affected by fluid viscosity. Farther downstream, viscous dissipation became more important.

The objective of this paper is to study planar-blast-wave propagation in an open-ended duct with emphasis on the flow structure associated with blast/vortex interaction, the mechanism of vorticity generation and acoustic-wave production, using a high-resolution Euler solver. Planar blast waves, which propagate downstream into a quiet air, are simulated by rupture of a high-pressure region located upstream. The numerical method used is the fifth-order weighted essentially nonoscillatory (WENO) scheme of Jiang and Shu.[10] To analyze the complicated flow structure, shadowgraphs, schlieren images, and interferograms images are generated from the computational results. The working fluid is air with $\gamma = 1.4$.

## II. Mathematical Formulation and Numerical Method

Based on the experimental data of Yang et al.,[2] the vortices caused by the shear layer are relatively small compared with the vortex generated by the diffracted shock wave. Therefore, we can reasonably assume that the flow is inviscid. The governing equations are the time-dependent Euler equations, which are nondimensionalized by the undisturbed flow conditions. The Cartesian coordinates $x$, $y$ are normalized by the horizontal-wall length $R$. The dimensionless time $t$ is normalized by $l/c_0$, where $l = R/40$, which is five times the thickness $(0.005R)$ of the high-pressure region, and $c_0$ is the sound speed of the undisturbed air. A schematic diagram of the flow problem and the computational domain with boundary conditions are shown in Fig. 2.

The initial conditions and values of flow parameters used in numerical simulation are listed in Table 1. In Table 1 $M_s$ denotes the Mach number of the blast-wave front at the 90-deg corner; $P_1/P_0$ the pressure ratio of the high-pressure $P_1$ to the lower pressure $P_0$ as shown in Fig. 2; and $t_1$, $t_2$ the dimensionless arrival times of the first and second shocks at the corner. The instant at which the high-pressure region starts collapsing is set to be $t = 0$. The subscript 1 denotes the flow properties of the high-pressure region, and 0 for the flow properties of the undisturbed air. Initially, the flow is stagnant, and the temperature is kept the same both in the high- and low-pressure regions. Figures 3a and 3b show the pressure distributions at the instants of $t_1$ and $t_2$ for the cases listed in Table 1. The second shock $S_2$ is much weaker than the primary shock $S_1$ because it has pressure ratios less than 1.2 and Mach numbers less than 1.05 at the instant $t_2$ for all cases. To ensure that the acoustic waves have enough space to propagate, the computational domain after normalization by $R$ is chosen to be $\{(x, y)| -1 \le x \le 1, -2 \le y \le 0\}$ with

**Table 1 Initial conditions used for numerical simulation**

| Blast Mach number $M_s$ | $P_1/P_0$ | $t_1$ | $t_2$ |
|---|---|---|---|
| 1.1 | 5.5 | 18 | 22 |
| 1.2 | 16 | 16 | 24 |
| 1.3 | 30 | 14 | 27.5 |
| 1.4 | 49 | 13 | 30 |
| 1.5 | 72 | 12 | 36 |

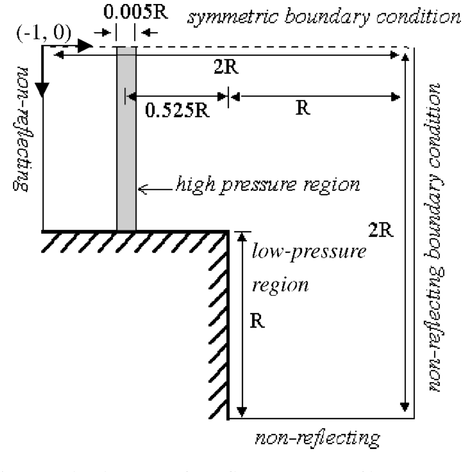

**Fig. 2 Schematic diagram of the flow problem of interest and the computational domain with boundary conditions.**

800 × 800 uniform grid points. The high-pressure region is located at a distance of 0.525 from the corner. This distance is enough to produce a completed blast wave. A high-order numerical method developed by Chen and Liang is used for solving the Euler equations. For spatial derivatives a fifth-order WENO scheme of Jiang and Shu[10] is adopted, and a fourth-order Runge–Kutta method is used for time integration. In our simulation a wave-nonreflecting two-dimensional boundary condition of Thompson[11] is imposed on the inlet and outlet boundaries. To save computational time and computer memory, only the lower half-domain is computed. The present code had been applied successfully to compute the flowfield of planar blast/vortex interaction, which includes acoustic waves, and the detailed flow structures as reflected shock waves, slip lines, and contact surfaces.[12] In addition, we compare the wall shock Mach number between numerical and experimental results. As presented in Table 2, our results show that good agreement is obtained.

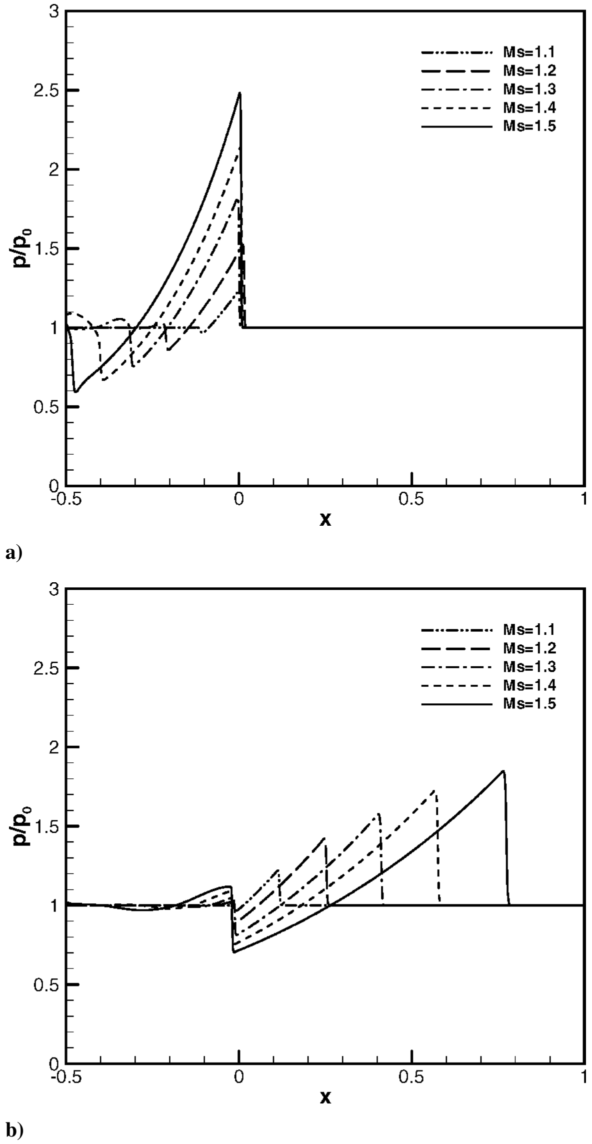

Fig. 3 Pressure distributions for different blast intensities at the instants of a) $t_1$ and b) $t_2$ listed in Table 1.

## III. Results and Discussion

### A. Flow Structure

For several decades experimental interferograms, schlieren, and shadowgraphs have been used to quantitatively and qualitatively study a compressible flow. Modern computer postprocessing techniques can now be used to create equivalent images, based on computed data. To study the complicated flow structures induced by the planar blast waves discharging from the duct exit, computational shadowgraphs, schlieren pictures, and interferograms are generated. By varying the pressure ratio ($P_1/P_0$), the blast waves with different intensities are generated. Figure 4 shows a schematic diagram of a planar blast wave discharging from an open-ended duct at different times. Figure 4a shows the produced blast wave that includes the primary shock $S_1$ and the second shock $S_2$. Figure 4b shows that the primary shock $S_1$ has passed the corner and a major vortex $V_1$ is generated and rotates in a clockwise direction. In addition to the major vortex, there is a smaller weak vortex $V_2$, which rotates in a counterclockwise direction. These two vortices are coupled together. The formation of this weak vortex is caused by the expansion wave $EW_1$. The whole wave pattern includes the incident shock $S_1$, diffracted shock $D_1$, expansion wave $EW_1$, and the contact surface $CS_1$. After the second shock passing through the corner, the expansion wave $EW_2$ and the contact surface $CS_2$ associated with the second shock $S_2$ are shown in Fig. 4c. The minor vortex $V_2$ grows as large as the major vortex after the second-shock diffraction. Figures 5a–5d show the computational shadowgraphs for $M_s = 1.3$ at dimensionless $t = 26$, 28, 32, 36, and Figs. 5e–5h for $M_s = 1.5$ at $t = 32$, 36, 42, 46. In Figures 5a and 5e one can clearly see the primary shock $S_1$, having passed the corner, the expansion wave front $EW_1$, the diffracted shock, the contact surface $CS_1$, the induced vortex $V_1$, and the second shock $S_2$. Figures 5b and 5f show the primary shock $S_2$ interacting with the vortex $V_1$. The expansion wave front $EW_2$ is formed, and the minor vortex $V_2$ is well developed. In Figs. 5c and 5g the second shock/vortex interaction is finished. The vortex pair $V_1$ and $V_2$ and the pair of contact surfaces $CS_1$ and $CS_2$ are

**Table 2 Comparison of computed values of the wall shock Mach number with experimental data**

| Wall shock Mach number $M_w$ | Shock Mach number $M_s$<br>Case 1: $M_s = 1.5$ | Case 2: $M_s = 2.0$ |
|---|---|---|
| Numerical value | 1.12 | 1.26 |
| Experimental value | 1.15 | 1.3 |
| Error, % | 2.5 | 3.1 |

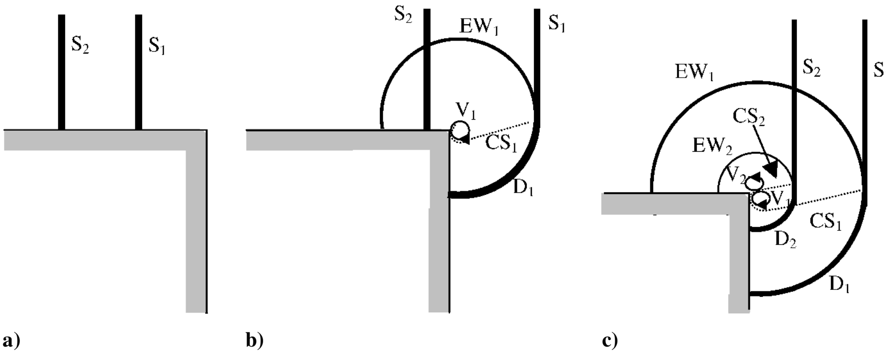

Fig. 4 Wave patterns of a planar blast wave discharging from an open-ended duct at different instants.

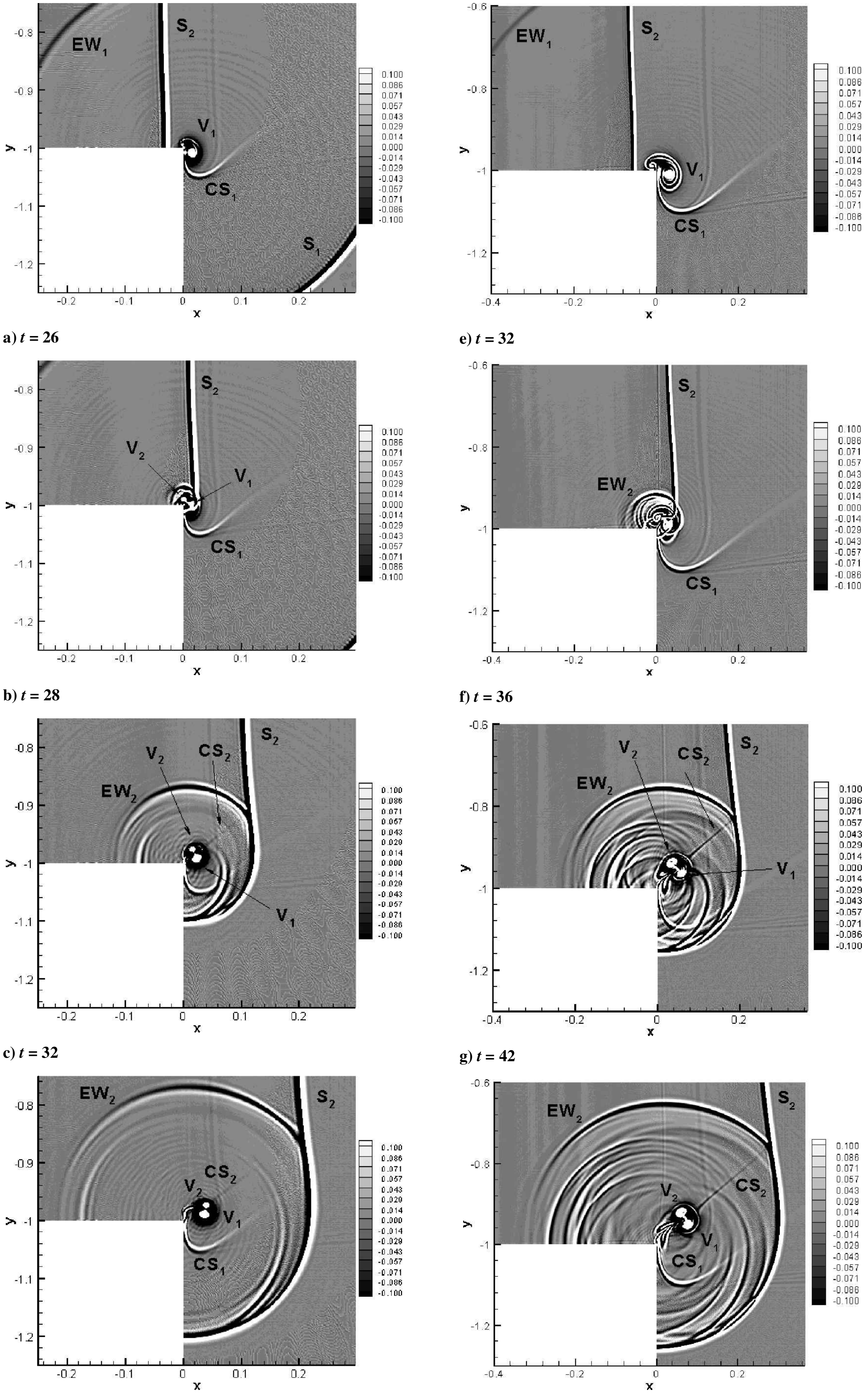

a) $t = 26$

b) $t = 28$

c) $t = 32$

d) $t = 36$

e) $t = 32$

f) $t = 36$

g) $t = 42$

h) $t = 46$

**Fig. 5 Computational shadowgraphs at different instants for a–d) $M_s = 1.3$ and e–h) $M_s = 1.5$.**

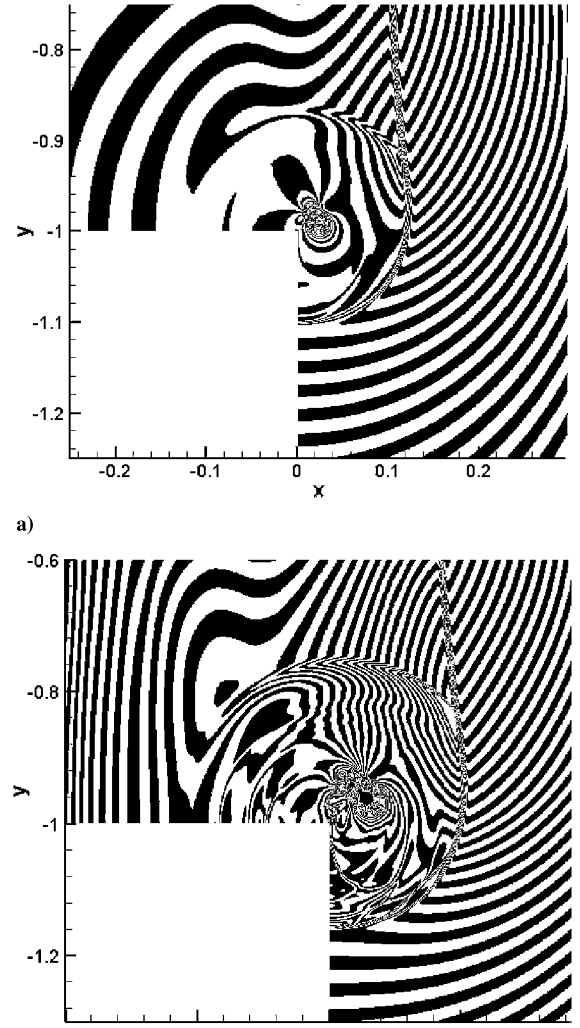

b)

**Fig. 6 Computational interferograms for a) $M_s$ = 1.3, $t$ = 36 and b) $M_s$ = 1.5, $t$ = 42, and $\Delta\rho$ = 0.005.**

completely formed. Another flow phenomenon of interest is the generation of acoustic waves caused by shock/vortex interactions in both cases. In Figs. 5d and 5h the global flow phenomena are similar to those shown at the preceding instant. Figures 6a and 6b show the interferograms for the case of $M_s = 1.3$, $t = 36$ and for the case of $M_s = 1.5$, $t = 42$, respectively. In both cases the dimensionless density values range from 0.7 to 1.1 with 80 increments. The contact surface is not clearly seen in the blast-wave diffraction case, unlike the shock-wave diffraction case in Ref. 1. This is caused by the effect of expansion waves following the blast-wave front. The acoustic waves generated are visible in Fig. 6 as well as in Fig. 5. The acoustic waves are better visualized by shadowgraphs than interferograms. If we disregard the accompanying second shock and its associated flow structure, the flowfields after blast-wave diffraction are similar to those in the shock-wave diffraction case. Plotting the position of the two vortices at different instant in times, as shown in Fig. 7, reveals that the vortex pair rotates cyclically in the clockwise direction.

## B. Sound Generation

The acoustic waves caused by the blast/vortex interaction are complicated, in particular, in the near field of the open-ended duct exit. The shadowgraphs and schlieren pictures can provide clear flow structures for qualitative analysis, and interferograms can be used for quantitative analysis. To recognize the rarefaction and compression phases, we use schlieren pictures for analyzing the acoustic waves. Figure 8 shows the computational schlieren pictures for the $M_s = 1.3$ and 1.5 cases at the same instants as in Fig. 5. In Fig. 8 the bright regions represent the compression (+) phase, and the dark regions represent the rarefaction (−) phase. Note that the contact surfaces, expansion waves, and acoustic waves (denoted by symbols + and −) can be seen clearly. Moreover, we can count the number of compression and rarefaction phases in the radial direction for the cases of $M_s = 1.3$ and 1.5. From Figs. 8b and 8d, we find that there is only one phase either rarefaction or compression in the case of $M_s = 1.3$ but three phases in the $M_s = 1.5$ case. Although the number of phases are different in the $M_s = 1.3$ and 1.5 cases, the sound wave is interlaced by the compression and rarefaction phases as shown in Figs. 8a–8d. It is known that, for a shock/vortex interaction in a free space, the sound wave generated is of quadrupolar nature. In the present cases one compression/rarefaction phase is generated and seems like dipole nature for the $M_s = 1.3$ case, as shown in Figs. 8a–8b. For the $M_s = 1.5$ case three phases (either two compressions and one rarefaction or two rarefactions and one compression) are generated, and the sound wave seems like tripole nature, as seen from Figs. 8c and 8d. It is evident that the number of interlaced compression/rarefaction phases generated depends on the blast intensity. Moreover, the geometric constraint of the duct might have an effect on the sound nature.

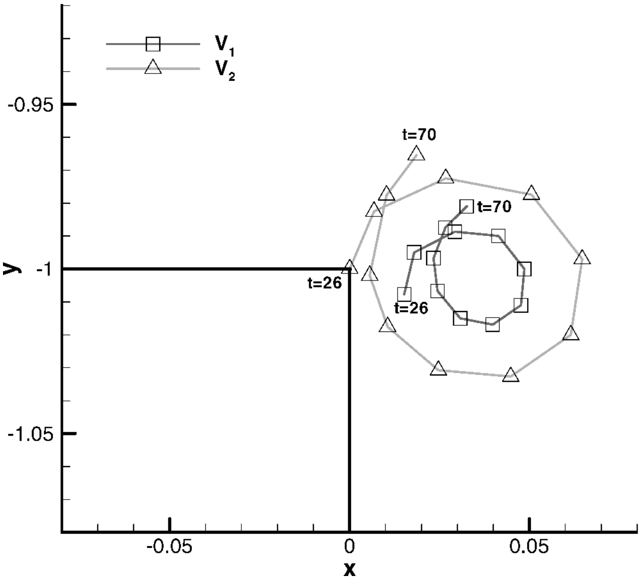

**Fig. 7 Trajectory of vortices $V_1$ and $V_2$ from $t$ = 26 to 70 with time increment, $\Delta t$ = 4 for the $M_s$ = 1.3 case.**

In our computations there is only one compression/rarefaction phase involved in sound generation for $M_s = 1.1$, 1.2. 1.3, but three phases for $M_s = 1.4$, 1.5. In the former cases the strength of the induced vortices and the second shock are weak; their interaction produces only one compression/rarefaction phase. In the latter cases the interaction is stronger, resulting in more compression/rarefaction phases because of the stronger vortices and the stronger second shock.

## C. Vorticity Production

The vorticity production induced by the blast-wave diffraction around the corner is governed by the vorticity transport equation of an inviscid flow:

$$D\omega/Dt = -\omega(\nabla \cdot V) - (\nabla p \times \nabla \rho)/\rho^2$$

where the vorticity $\omega$ is the curl of the velocity, $\nabla$ the gradient operator, $\rho$ the density, and $p$ the pressure. The first term in the right-hand side is called the compressibility term and denotes the roll up of the slipstream scaled up by the fluid dilatation (the compressibility effect). The second term, called the baroclinic term, denotes the baroclinic effect of misalignment of the pressure and density gradients. Abate and Shyy[9] mention that in the case of a

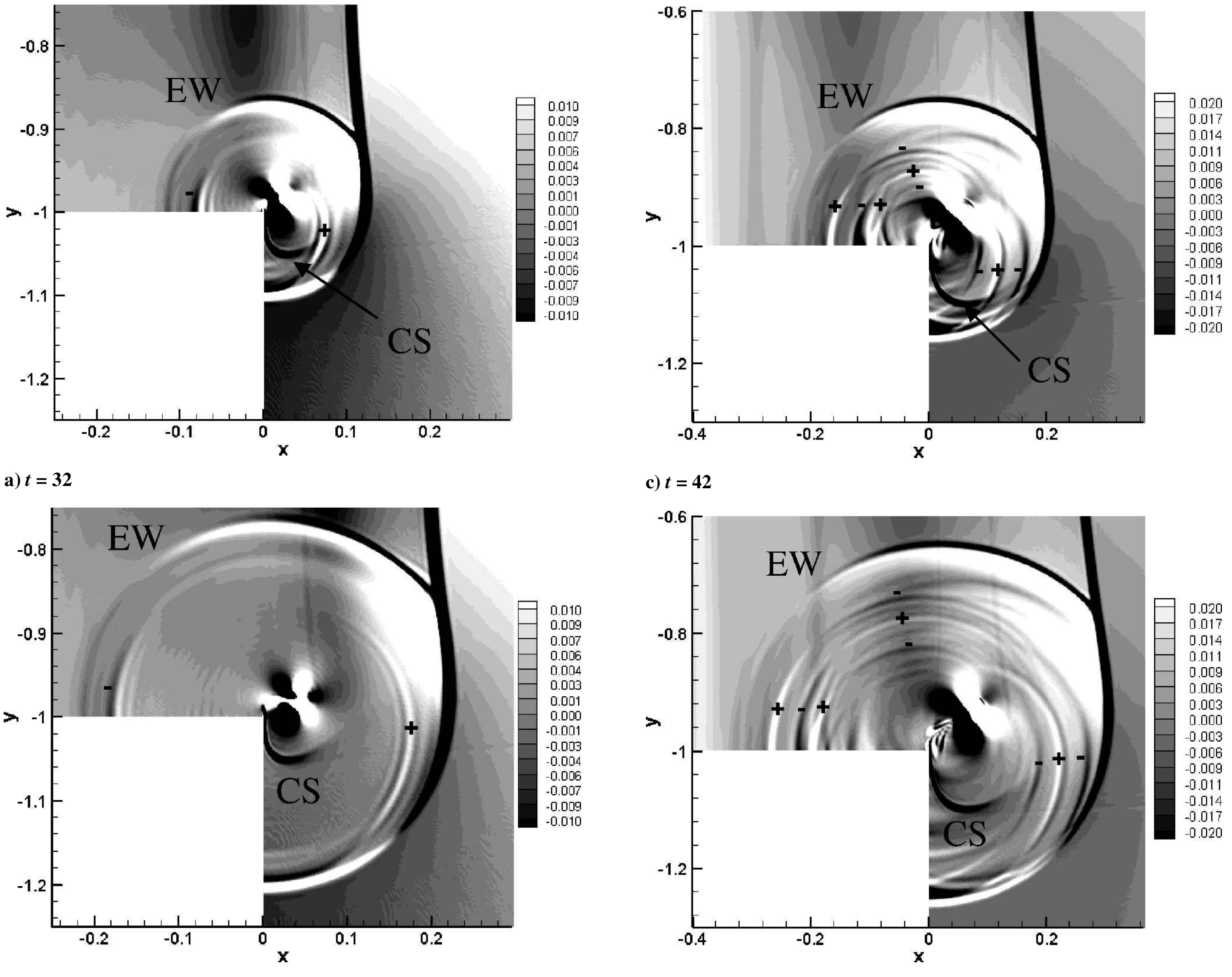

a) $t = 32$

c) $t = 42$

b) $t = 36$

d) $t = 46$

**Fig. 8 Computational schlieren pictures at different instants for a, b) $M_s$ = 1.3 and c, d) $M_s$ = 1.5.**

shock passing through a sharp corner vorticity generation is dominated by the baroclinic effect. It is desired to identify the dominant factor for vorticity production in the case of blast-wave diffraction. Moreover, we would like to clarify the growth process of the induced vortices. The vorticity contours corresponding to Fig. 5 are shown in Fig. 9. Figure 9a shows both vortices at the beginning of the interaction. The newly developed vortex $V_2$ is much smaller than $V_1$. Later, the minor vortex grows quickly; however, the major vortex size remains almost the same, as shown in Figs. 9b and 9c. At $t = 36$ the minor vortex has developed to almost the same size as the major vortex with the same order of the maximum vorticity, as shown in Fig. 9d. For the case of $M_s = 1.5$ (the second case), the evolution of the minor vortex is similar to that in the first case. However, the two vortices are much stronger than those in the first case, as shown in Figs. 9e–9h, as a result of the stronger blast wave.

We further explore the flow structure in detail by comparing Fig. 5 with Fig. 9. The primary shock wave $S_2$ interacts with the two vortices $V_1$ and $V_2$ at $t = 26$ for the $M_s = 1.3$ case and $t = 32$ for $M_s = 1.5$ case. The minor vortex $V_2$ reaches the maximum positive vorticity at the instant when the second shock arrives near the minor vortex in which the negative phase of the blast profile is most influential, as shown in Figs. 9a and 9e. Later, the second shock and the minor vortex interact with each other. The maximum vorticity of the minor vortex is decreased because the vortex-center pressure is increased because of the effect of the second shock, as shown in Figs. 10b and 10f. At this instant ($t = 28$ for the $M_s = 1.3$ case and $t = 36$ for $M_s = 1.5$ case) the major vortex $V_1$ reaches the maximum vorticity (a negative value). This is a resultant effect of the expansion phase of the blast profile. The expansion phase contains the positive- and negative-pressure phases. After the interaction the minor vortex grows because of vorticity diffusion. The maximum vorticity of the minor vortex is almost the same order of magnitude as that for the major vortex, as indicated in the value indicator in Figs. 9c and 9d and 9g and 9h.

To understand the mechanisms of vorticity generation, the contributions as a result of the fluid compressible and baroclinic terms for the $M_s = 1.3$ case are shown in Fig. 10. Figures 10a–10d show the contributions of the compressibility term to vorticity production at $t = 26$, 28, 32, 36, and Figs. 10e–10h for the baroclinic term. In Figs. 10a and 10b and Figs. 10e and 10f the maximum negative and positive values of the compressibility term are about one order of magnitude larger than those for the baroclinic term during the second shock interacting with the two vortices. Both the maximum positive and negative values of these two terms at these instants are of the same order of magnitude during the interaction. After the interaction the values of the compressibility term decrease from $t = 32$ to 36, but not the baroclinic term that remains the same magnitude, as shown in Figs. 10c and 10d, and 10g and 10h. This is mainly caused by the values of the fluid dilatation ($\nabla \cdot \boldsymbol{V}$) are changed to small values after the interaction (from $t = 32$ to 36). By comparing the magnitudes of these two terms as shown in Fig. 10, we can see that the contribution of the compressibility term to vorticity production is much more than the baroclinic term. We found that the values of the compressibility term resulted from large values of vorticity

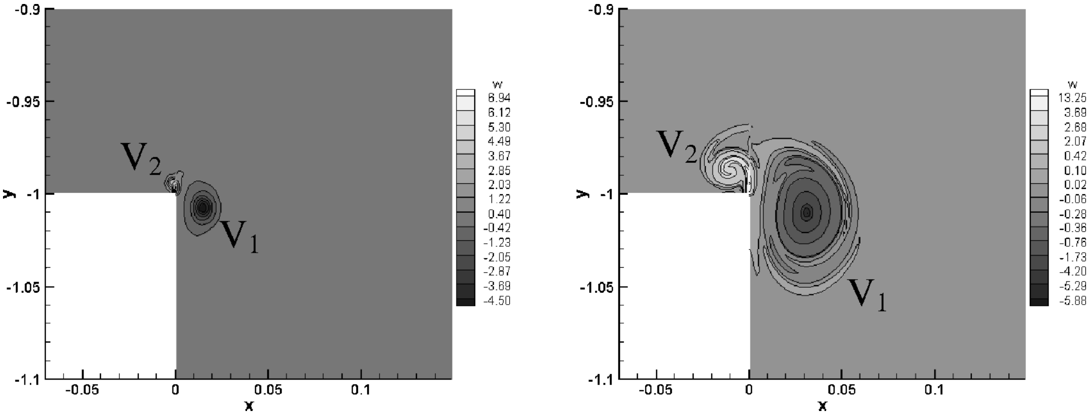

a) *t* = 26

e) *t* = 32

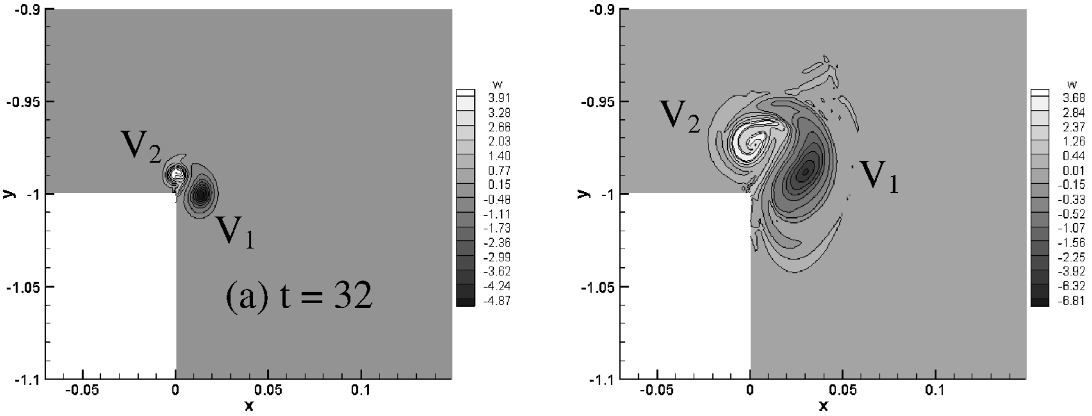

b) *t* = 28

f) *t* = 36

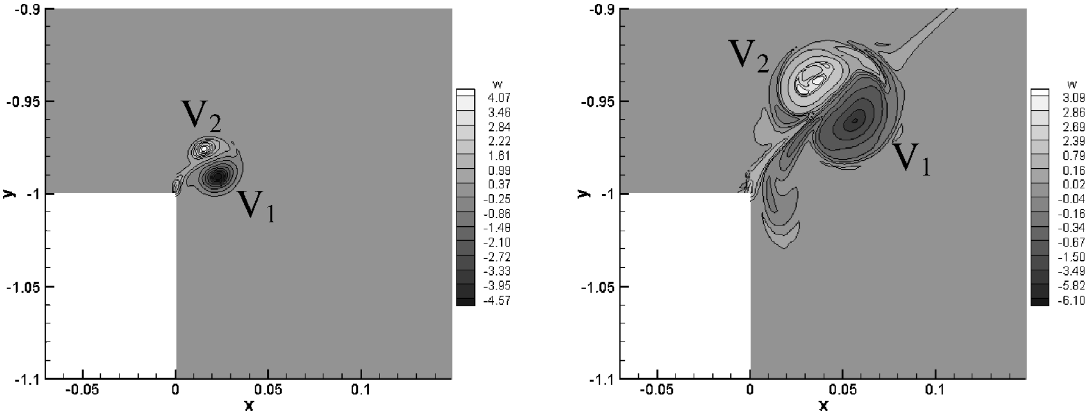

c) *t* = 32

g) *t* = 42

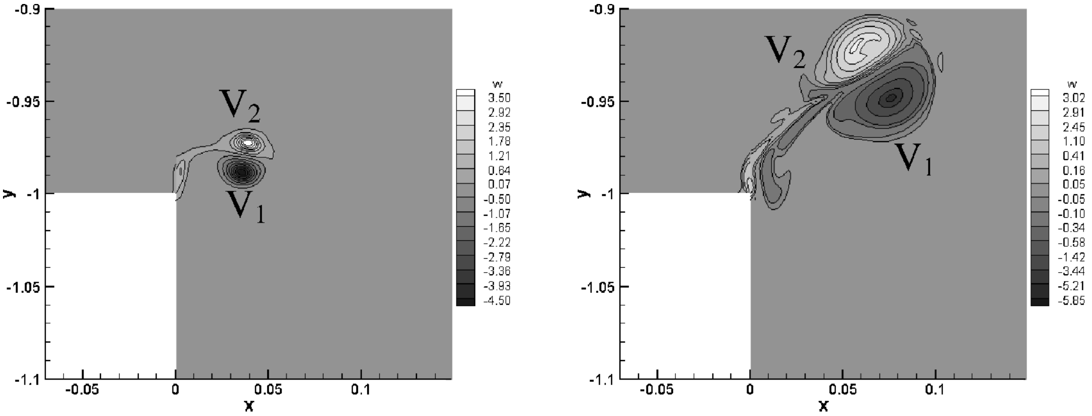

d) *t* = 36

h) *t* = 46

**Fig. 9 Vorticity contours at different instants: a–d) $M_s = 1.3$ and e–h) $M_s = 1.5$.**

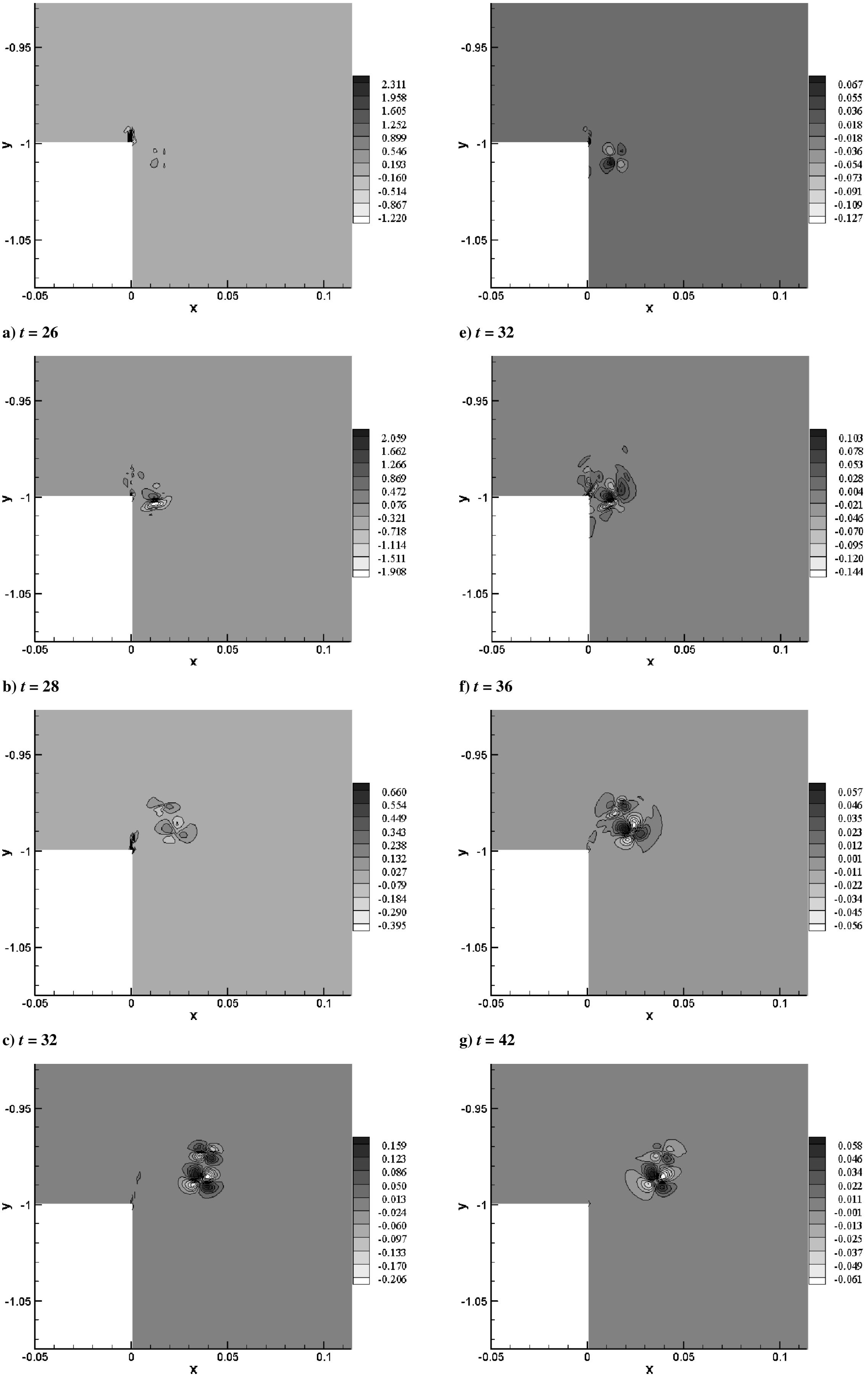

**a)** $t = 26$

**b)** $t = 28$

**c)** $t = 32$

**d)** $t = 36$

**e)** $t = 32$

**f)** $t = 36$

**g)** $t = 42$

**h)** $t = 46$

**Fig. 10 Contributions caused by a–d) the fluid compressibility and e–h) baroclinic terms for the $M_s = 1.3$ case at different instants.**

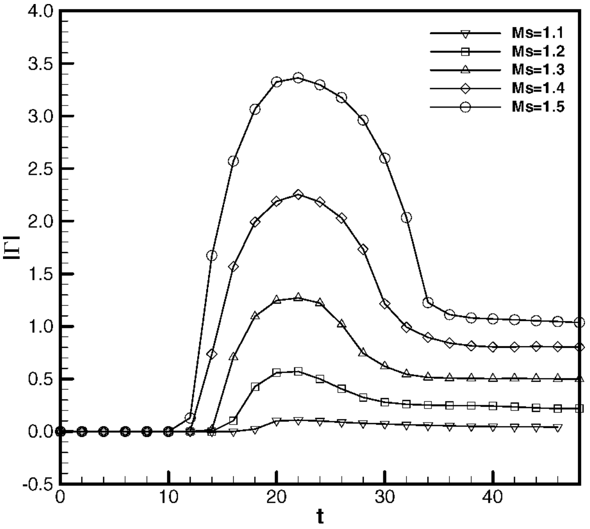

**Fig. 11 Circulation (in absolute value) of the two vortices vs time for different blast intensities.**

$\omega$, which was a result of the roll up of the slipstream, scaled down by small values of the fluid dilatation $(\nabla \cdot \boldsymbol{V})$. The discounting of original values of the vorticity can be interpreted as the fluid dilatation suppresses the vorticity generation. Hence the baroclinic effect is still much more effective than the dilatation effect or the compressibility effect. In summary, the compressibility term plays more important role in the vorticity production than the baroclinic term in the case of blast-wave diffraction around a sharp corner. The vorticity generated by the first shock mainly contributes the values of the compressibility term, $-\omega(\nabla \cdot \boldsymbol{V})$.

For the invisvid flow the circulations (in absolute value) of the two vortices vs time for different blast-wave intensities are shown in Fig. 11. The circulation increases to a maximum value when the second shock begins to interact with the major vortex $V_1$. After the second shock/major vortex interaction the circulation decreases to a constant value. Namely, when the blast wave moved away from the vortices, there is no additional kinetic energy imparted to the flow.

## IV. Conclusions

By employing a fifth-order weighted essentially nonoscillatory scheme to solve the two-dimensional, unsteady compressible Euler equations, the flowfields of planar blast waves with different intensities discharging from an open-ended duct have been studied. The acoustic waves and a vortex pair generated by blast/vortex interactions at different blast Mach numbers are investigated by using computational shadowgraghs, schlieren pictures, and interferograms. It is found that the number of sound is dependent on the strength of the blast wave. The mechanism of vorticity generation induced by blast-wave diffraction around the 90-deg corner is studied in detail. The second shock/vortex interaction plays an important role in the vorticity generation process. The compressibility term is more dominant than the baroclinic term in the vorticity transport equation during the second shock/vortex interaction. The roll up of the slipstream mainly contributes the values of the compressibility term. The baroclinic effect is much more effective than the dilatation effect $(\nabla \cdot \boldsymbol{V})$ during second shock/vortex interaction by comparing their order of magnitude. In addition, it is found that the circulation (or strength) of the two vortices is constant when the incident blast wave has moved far downstream.

## Acknowledgments

The support for this study under Grant NSC 90-2213-E006-096is gratefully acknowledged. The authors thank M. Platzer for reading the manuscript.

## References

[1] Hillier, R., "Computation of Shock Wave Diffraction at a Ninety-Degree Convex Edge," *Shock Waves*, Vol. 1, No. 2, 1991, pp. 89–98.

[2] Yang, J., Kubota, T., and Zukoski, E. E., "An Analysis and Computational Investigation of Shock-Induced Vortical Flows," AIAA Paper 92-0316, Jan. 1992.

[3] Yates, L. A., "Images Constructed from Computed Flowfields," *AIAA Journal*, Vol. 31, No. 10, 1993, pp. 1877–1884.

[4] Yu, Q., and Grönig, H., "Shock Waves from an Open-Ended Shock Tube with Different Shapes," *Shock Waves*, Vol. 6, No. 5, 1996, pp. 249–258.

[5] Inoue, O., and Hattori, Y., "Sound Generation by Shock-Vortex Interactions," *Journal of Fluid Mechanics*, Vol. 380, Feb. 1999, pp. 81–116.

[6] Kim, H. D., and Setoguchi, T., "Study of the Discharge of Weak Shocks from an Open End of a Duct," *Journal of Sound and Vibration*, Vol. 226, No. 5, 1999, pp. 1011–1028.

[7] Jiang, Z., and Takayama, K., "An Investigation into the Validation of Numerical Solutions of Complex Flowfields," *Journal of Computational Physics*, Vol. 151, No. 2, 1999, pp. 479–497.

[8] Szumoswki, A., Sobieraj, G., Selerowicz, W., and Piechna, J., "Starting Jet-Wall Interaction," *Journal of Sound and Vibration*, Vol. 232. No. 4, 2000, pp. 695–702.

[9] Abate, G., and Shyy, W., "Dynamic Structure of Confined Shocks Undergoing Sudden Expansion," *Progress in Aerospace Sciences*, Vol. 38, No. 1, 2002, pp. 23–42.

[10] Jiang, G.-S., and Shu, C.-W., "Efficient Implementation of Weighted ENO Schemes," *Journal of Computational Physics*, Vol. 126, No. 1, 1996, pp. 202–228.

[11] Thompson, W., "Time Dependent Boundary Conditions for Hyperbolic Systems," *Journal of Computational Physics*, Vol. 68, No. 1, 1987, pp. 1–24.

[12] Chen, H., and Liang, S. M., "Planar Blast/Vortex Interaction and Sound Generation," *AIAA Journal*, Vol. 40, No. 11, 2002, pp. 2298–2304.

M. Sichel
*Associate Editor*